Earth and Planetary Science Letters xxx (xxxx) 118595

Contents lists available at ScienceDirect

Earth and Planetary Science Letters

journal homepage: www.elsevier.com

Seismo-turbidites reveal locations of major earthquakes during the past millennium in the Gulf of Aqaba, southern Dead Sea fault

Zeynep Bektaş [a, *], Ulaş Avşar [a], Matthieu Ribot [b], Yann Klinger [c], Sigurjón Jónsson [b]

[a] Department of Geological Engineering, Middle East Technical University, 06800 Ankara, Turkey
[b] Physical Science and Engineering Division, King Abdullah University of Science and Technology (KAUST), Thuwal 23955, Saudi Arabia
[c] Université Paris Cité, Institut de Physique du Globe de Paris, CNRS, F-75005 Paris, France

ARTICLE INFO

Editor: J.P. Avouac

Keywords:
Paleoseismology
Seismo-turbidites
Recurrence interval
Earthquake
Sedimentary sequence
Radiographic images

ABSTRACT

Although ample historical and paleoseismological information is available on major past earthquakes along the onland part of the Dead Sea Fault, knowledge of the seismic behavior of its southernmost part in the Gulf of Aqaba has remained limited. To fill this gap and improve our understanding of the seismic potential of the submarine faults in the gulf, we analyzed 18 sediment cores ranging in length from 26.8 to 107.3 cm for sedimentary traces of past earthquakes. Radiographic images of the cores reveal numerous well-preserved turbidites intercalated within bioturbated background sediments. In addition, we used magnetic susceptibility, grain-size and μ-XRF data to detect instantaneous deposition in the sedimentary sequence and stratigraphically correlate the cores along the gulf. These results show coevality of some of the turbidites in cores from different basins of the gulf, which we used as the criterion to assign seismic origin for turbidites. In the top ~1000 years of the sedimentary sequence, where the spatio-stratigraphical correlations are robust, seismo-turbidites caused by the known earthquakes of 1068, 1212, 1588, 1839, and CE 1995 were successfully detected. We found seismo-turbidites triggered by the 1995 earthquake only in the northern half of the gulf, confirming that this part of the fault system ruptured in 1995. On the other hand, the earthquakes in 1068 and CE 1588 triggered turbidites throughout the gulf, indicating that the entire fault system in the gulf was activated during these earthquakes. In addition, we detected seismo-turbidites of the 1212 and CE 1839 earthquakes only locally, suggesting these were smaller earthquakes. One core containing a sedimentary sequence back to ~1800 BCE shows likely seismo-turbidites around CE 363, 250 BCE, 850 BCE and 1350 BCE. Together with the 1588 and 1068 earthquakes, these older possible seismo-turbidites may indicate a 400–700 (average = 560) year recurrence interval for large earthquakes in the gulf. Absence of significant turbidites in the southern gulf since CE 1588 therefore implies that this part of the fault system could be a candidate for a large earthquake in the near future.

1. Introduction

Determining the location, timing, and size of devastating earthquakes in the past plays a key role in understanding active fault behavior and recurrence interval of large events and to mitigate future losses due to seismic hazard. On-fault trenching, which mainly aims at detecting and dating past surface rupturing events in faulting-related sedimentary sequences, is the most frequently used method in paleoseismological investigations (Kelsey et al., 1998; Masana et al., 2004; McCalpin, 2009; Avşar et al., 2014; Klinger et al., 2015). However, if active fault segments are submerged, like in the case of the North Anatolian Fault in the Marmara Sea or the Dead Sea Fault in the Gulf of Aqaba, on-fault trenching is impracticable (Avşar et al., 2014). In such areas, marine paleoseismological techniques are required. Hence, turbidites (Goldfinger, 2009; 2011; Patton et al., 2013; 2015; Moernaut et al., 2014; Van Daele et al., 2014; Avşar et al., 2015; Ikehara et al., 2016; Goldfinger et al., 2017; Polonia et al., 2017; 2023; Usami et al., 2018; Wils et al., 2021) and soft sediment deformations (Monecke et al., 2004; Avşar et al., 2016; Molenaar et al., 2021; 2022) are the main sedimentary fingerprints that are used to understand the paleoseismic history of faults.

During an earthquake, sediment stability on subaqueous slopes can be lost due to the intensity of ground shaking. Dense clouds of wasted sediment are transported along slopes and finally get deposited in the middle parts of basins. Therefore, earthquake-induced subaqueous mass wasting events are captured as intercalations of "seismo-

* Corresponding author.
E-mail address: zbektas@metu.edu.tr (Z. Bektaş).

https://doi.org/10.1016/j.epsl.2024.118595
Received 17 July 2023; Received in revised form 26 November 2023; Accepted 24 January 2024
0012-821/

turbidites" within the background sedimentation of the basins. However, it is important to be aware that earthquakes are not the only source for turbidites. Any natural event that causes ground shaking, flooding, and over-steepening of subaqueous slopes due to continuous sedimentation can also trigger mass wasting (Goldfinger et al., 2007; Avşar et al., 2015; Molenaar et al., 2021). Hence, to ascertain the seismic origin of a turbidite sequence, it is critical to investigate the spatial and temporal extent of turbidites because the probability that mass-wasting events get triggered simultaneously along different slopes in different basins (or in isolated depocenters) by any processes other than earthquakes is very low. In addition, the temporal correlation of the observed turbidites with historically and/or instrumentally recorded earthquakes helps to understand the effects of seismic shaking on sedimentary processes in the geologic setting under consideration, so that more reliable paleoseismic interpretations can be made for the prehistorical periods in sedimentary sequences (Fanetti et al., 2008; Avşar, 2013).

Although there are well-acknowledged paleoseismic data along the Dead Sea Fault system from on-fault trenching studies, the behavior of the fault system in the Gulf of Aqaba has remained mostly unknown due to lack of submarine paleoseismological data. To address this problem, we investigated 18 sediment cores taken from the different basins of the gulf (Fig.1a). In addition to the 1995 (Mw 7.2) earthquake in the gulf, historical knowledge from the old cities of Aqaba and Eilat, and the St. Catherine's Monastery on the southern Sinai Peninsula states that the Gulf of Aqaba region was affected by strong earthquakes in 1068, 1212, and CE 1588 (Ambraseys, 2009). Sedimentary consequences of these earthquakes allowed us to evaluate the sensitivity of the sedimentary processes in the gulf to seismic activity, and hence to better understand the behavior of the Dead Sea Fault in the area.

2. Study area and on-shore paleoseismology

The Gulf of Aqaba is located at the northern end of the Red Sea. It separates the Arabian plate and Sinai microplate by trans-tensional deformation along the southernmost part of the ~1000-km-long left lateral strike-slip Dead Sea Fault (Ribot et al., 2021). The Gulf of Aqaba, which is approximately 180 km long and 25 km wide at its widest consists of four pull-apart basins or deeps (Ben-Avraham et al., 1979; Z. 2008; Tibor et al., 2010; Ribot et al., 2021); namely from north to south, Eilat (average depth: D_{avg}: 900 m), Aragonese (D_{avg}: 1750 m), Dakar (D_{avg}: 1250 m) and Tiran (D_{avg}: 1280 m) deeps. Trans-tensional deformation also formed the Hume deep (D_{avg}: 1400 m), which is located just south of the Strait of Tiran. Four main transform fault segments bound the basins in the gulf in a left-stepping en echelon arrangement (Fig. 1b). These faults from north to south are the Eilat, Aragonese, Arnona and Tiran faults. In addition, several secondary dip-slip faults also contribute to the morphology of the Gulf of Aqaba. The Aragonese fault and probably partially the Eilat fault ruptured during the 1995 M_w7.2 Nuweiba earthquake (Klinger et al., 1999; Ribot et al., 2021).

The Wadi Araba Fault (Fig. 1b) is the southernmost on-land segment of the Dead Sea Fault system and it runs between the Dead Sea and the Gulf of Aqaba, entering into the gulf at the location of the city of Eilat. A series of paleoseismic trenches from Rahma in the north to Eilat in the south (see location in Fig. 1b: x, y, z, and t) were studied to examine the Wadi Araba Fault in detail. Klinger et al. (2015) excavated a trench at the Qatar Site (x in Fig. 1b) and they identified nine distinct surface rupturing events. However, only five events, in 363, 8th century, 1068, 1212 and CE 1458, can be tied to historical earthquakes. Conversely, evidence of some major historical events could not be found at this site, such as of the CE 1588 earthquake, which impacted a large area, from Madinah to Cairo. Accordingly, Klinger et al. (2015) concluded that the 1588 earthquake probably occurred further south in the Gulf of Aqaba. Traces of the CE 1293 and CE 1546 earthquakes, like the CE 1588 earthquake, were also not found at the Qatar site, but were found farther north and thus, these earthquakes were assigned to fault sections located directly south of the Dead Sea basin (Lefevre et al., 2018). Beyond the historical events, Klinger et al. (2015) also reported three prehistorical events, one in the period 338 - 213 BCE and two in the period 2797 - 1245 BCE.

Two paleoseismic investigations were carried out at the Avrona Site (y in Fig. 1b) by Amit et al. (1999) and Zilberman et al. (2005). Amit et al. (1999) claimed that at least six $M > 6$ earthquakes have affected the Avrona playa in the last 14,000 yrs, yielding an approximate recurrence interval of 2000 yrs. Although they do not report the dates of detected events one by one, Amit et al. (1999) assigned their youngest surface rupturing event to the CE 1212 earthquake. The paleoseismic trenches opened by Amit et al. (1999) were also used by Zilberman et al. (2005), who utilized in addition archaeological evidences to refine the date of the youngest surface rupturing event to be the CE 1068 earthquake, rather than the CE 1212 earthquake. They claimed that the CE 1212 earthquake must have been generated by a secondary fault on the eastern edge of the Eilat depression, rather than by the Wadi Arabah Fault. Furthermore, Amit et al. (2002) conducted a paleoseismic trenching study at the Shehoret Site (z in Fig. 1b), which is located southwest of the Avrona Playa. This study reports recurrence intervals of major earthquakes during the Late Pleistocene as 2.8 ± 0.7 ka and during the Holocene as 1.2 ± 0.3 ka.

In addition to the studies mentioned above, Kanari et al. (2020) carried out paleoseismic trenching on the southern section of the Wadi Arabah Fault in the Eilat Sabkha (t in Fig. 1b). They detected stratigraphical traces of surface rupturing and paleoliquefaction in the light of seismic reflection profiles and paleoseismic trenches. In addition to the ruptures of the historical CE 1068 earthquake, both rupturing and paleoliquefaction evidences were reported for an event that could be related to one of the historical earthquakes of CE 1458 or CE 1588. Although no direct surface rupturing was observed for the CE 1212 earthquake, a paleoliquefaction structure dated to before 1269–1389 CE in the Eilat Sabhka was attributed to this earthquake.

3. Methods

Prior to the sediment coring, we carried out a multibeam bathymetric survey using a Kongsberg EM 710-MK2 multi-beam echo sounder (R/V Thuwal cruise, 20 May – 7 June 2018) to reveal the morphology in the gulf and determine the core locations (Ribot et al., 2021). We then collected 18 short sediment cores of lengths from 28.6 cm to 107.3 cm during the same cruise from different basins of the gulf (Fig. 1, Table 1). Cores #11 and #13 were collected with a piston corer, while the other cores were collected by a multi-corer system, which ensures no sediment loss or disturbance at the water/sediment interface during coring. To analyze the cores, we used a range of methods. First, we carried out ITRAX μ-XRF scanning on 4.2 cm-wide and 0.8 cm-thick u-channels extracted from the cores, which provides much better radiographic images compared to scanning on half-cores. We then, by using a Mo tube, radiographically scanned at 0.2 mm resolution with 700 ms exposure time and used μ-XRF scanning at a resolution of 0.5 mm with an exposure time of 5 s. Furthermore, we performed magnetic susceptibility measurements at 0.5 cm intervals using a Bartington MS2E with point sensor. Finally, in order to determine the grain-size distribution along the cores, we sampled 1 cm-thick sediment slices in the u-channels and weighed them. The fractions coarser than 63 μm obtained by wet sieving were made carbonate-free by using 0.1 M HCl, and dried. The rate of dry carbonate-free fraction >63 μm to bulk wet sediment weight is reported as percentile profile of sand along the cores.

We built the sediment chronology by using radiocarbon (^{14}C) and radionuclide (^{210}Pb) dating from samples collected in core sections corresponding to regular background sedimentation. Excess of ^{210}Pb activity was measured for 10 samples (1 cm-thick) at the top parts of cores

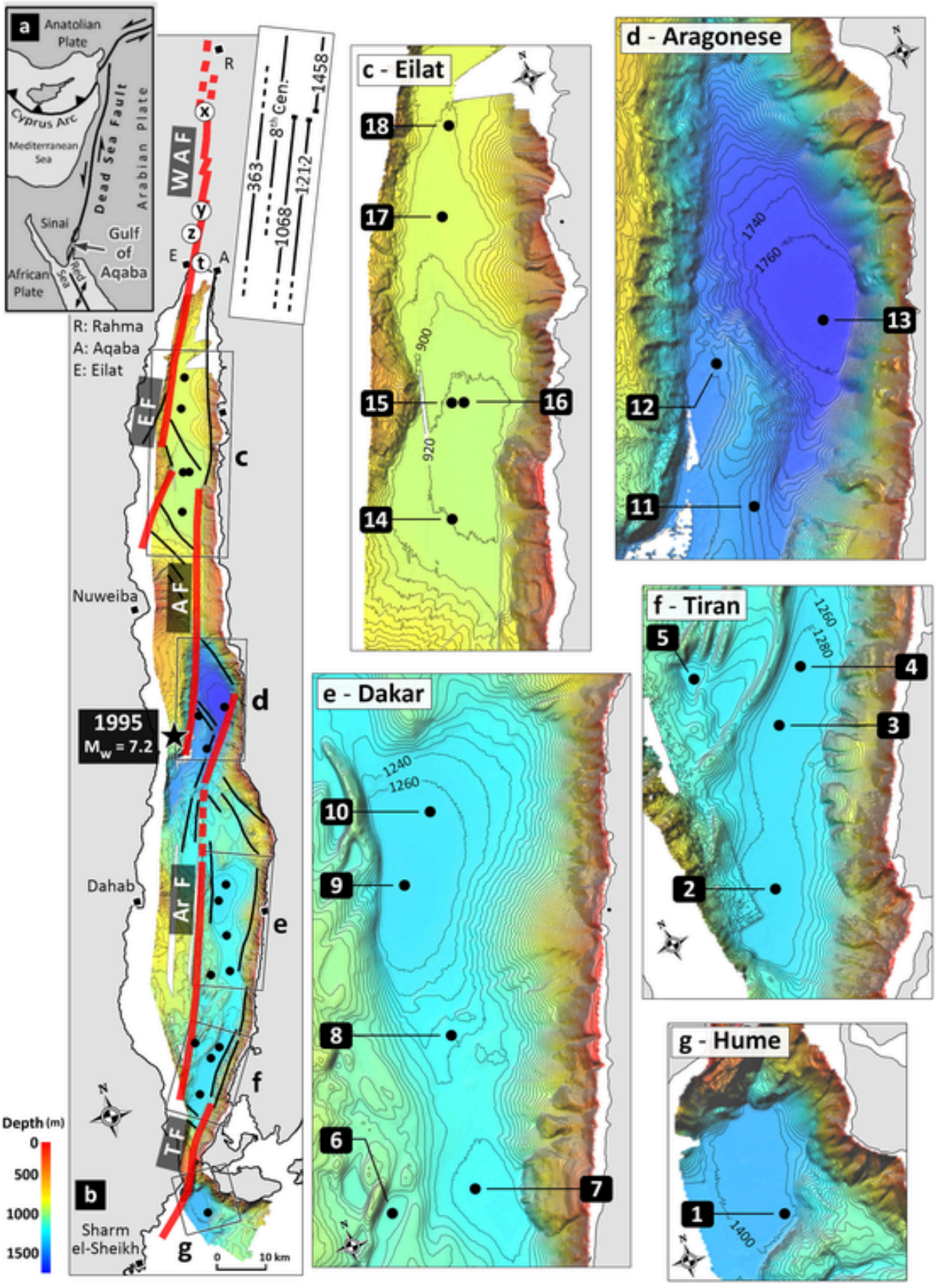

Fig. 1. Sediment coring locations in the Gulf of Aqaba. a) Tectonic setting in the eastern Mediterranean and the northern Red Sea. b) The bathymetry of the Gulf of Aqaba and active faults (Ribot et al., 2021; Le Béon et al., 2012) with black dots showing the coring locations. The main strike-slip faults are in red (TF: Tiran Fault, ArF: Arnona Fault, AF: Aragonese Fault, EF: Eilat Fault, WAF: Wadi Araba Fault) whereas normal faults are in black. Paleoseismic trenching sites are labelled as x

Fig. 1.—*continued*
(Klinger et al., 2015), y (Amit et al., 1999; Zilberman et al., 2005), z (Amit et al., 2002), and t (Kanari et al., 2020). The top right inset shows the lateral extent of historical earthquakes on the WAF (Klinger et al., 2015). c-g) Close-up views of the coring locations in the Eilat, Aragonese, Dakar, Tiran and Hume deeps.

Table 1
List of location coordinates (UTM Zone 36) and lengths of collected sediment cores.

Core	Easting (m)	Northing (m)	Length (cm)
1	644,865	3,088,436	45.9
2	649,077	3,111,652	47.4
3	652,978	3,117,903	49.4
4	655,166	3,119,657	49.1
5	650,794	3,121,557	50.1
6	657,203	3,133,933	50.6
7	661,076	3,133,747	50.5
8	662,336	3,140,643	28.6
9	662,551	3,147,720	48.5
10	664,713	3,150,458	50.1
11	668,163	3,177,363	107.3
12	668,282	3,184,094	44.4
13	673,361	3,184,597	71.5
14	675,592	3,224,035	50.4
15	677,936	3,231,543	55.6
16	678,437	3,231,416	34.2
17	680,724	3,243,846	44.0
18	682,879	3,249,608	38.5

#3, #7, and #17, by using a low-background, high-efficiency well-type gamma spectrometer (Schmidt et al., 2014). We then collected a total of 16 samples (1 cm-thick) from the u-channels of cores #3, #7, #9, #11, #13, #14, and #15 and wet sieved them for the fraction >63 μm, and manually picked up approximately 250 individuals of planktonic foraminifera (*Trilobatus sacculifer* (Brady, 1877) and *Globigerinoides ruber* (d'Orbigny, 1839)) under stereomicroscope and sent to the Poznan Radiocarbon Laboratory for radiocarbon dating. The raw ^{14}C results from foraminifera were calibrated by using the OxCal software (Version 4.4, Bronk Ramsey, 2001) according to the Marine20 calibration curve (Heaton et al., 2020) and the local radiocarbon reservoir age ($\Delta R = -31 \pm 21$), which was obtained from Calib.org website by averaging two ΔR values determined at Ras Umm Sid and Aqaba (Felis et al., 2004). We constructed an age-depth model by using the P_Sequence function of OxCal, which allows for fluctuations in sedimentation rate (Bronk Ramsey, 2008). The P_Sequence function also calculates the probability density functions (PDFs) for each sedimentary event according to the constructed age-depth model.

4. Results

4.1. Turbidites and sedimentary events

Radiographic images of the cores reveal that the background sediments in the Gulf of Aqaba do not exhibit lamination due to intense bioturbation (Figs. 2 and 3). Since the shell density of planktonic foraminifera (1.4 – 1.5 g/cm^3, Be, 1959; Fok-Pun and Komar, 1983) is generally lower than that of the sediments, they are seen in the radiographic images as light-colored spots. Within the intensely bioturbated background sediments having high biogenic content (predominantly planktonic foraminifera), we identified numerous sedimentary anomalies that are significantly different from these complex background sediments in our cores. These sedimentary anomalies, which produce signals that differ significantly from the background sediments in proxies and radiographic images, are labeled alphabetically from the top to the bottom for each core (Figs. 2, 3, and 4). They appear in the radiographic images as darker intercalations, implying that they have higher density compared to the background sediments.

The examples of the sedimentary events presented in Fig. 2 are the most prominent and well-preserved turbidites in the studied cores. Due to their instantaneous deposition and thickness mostly over 4 cm, bioturbation is limited to only the topmost parts of these turbidites, resulting in well-preserved internal structures. Parallel-to-subparallel laminations (Fig. 2: 2-E, 15-B, 3-A, 4-A, 15-C, 16-B, 17-G, and 15-A), and even cross laminations in some cases (3-E, 4-D, 14-B, and 16-A; Fig. 2), just above the sharp bottom boundaries of these events, can be attributed to multiple coarse sediment pulses that are due to multiple successive mass wasting events along basin slopes, likely caused by an earthquake (Shiki et al., 2000; Nakajima and Kanai, 2000; Goldfinger et al., 2007; C. 2008; Goldfinger, 2011; Van Daele et al., 2014; 2017; Wils et al., 2021). These distinct laminations are mostly overlapped by more homogeneous and probably finer-grained sediments that are clearly lacking carbonaceous biogenic content, i.e. mostly planktonic foraminifera, that show as whitish spots (e.g., 13-I in Fig. 2). Although boundaries at the bottom of turbidites are sharp and distinct, the boundary between the top of the turbidite and the above background sediments is difficult to determine precisely since it is gradational and bioturbated (C. Goldfinger et al., 2008; Goldfinger, 2011). In addition to their well-preserved internal structures, the lack of biogenic content in these sediments confirms their quasi-instantaneous deposition, which must have been too fast for the biogenic carbonates precipitating from the water column to be included into the sediments. In this study, we classify all of the sedimentary events that appear like the ones presented in Fig. 2 as "Type I: Turbidites".

Several events, like 2-B and 14-A in Fig. 3, have thick distinct multiple laminations and nondistinct foraminifera-free homogenous parts. On the other hand, events 1-C and 18-C also have thick distinct multiple laminations but have no homogenous parts. For some others, like 7-B, 7-D, 11-C, 11-J, and 17-A (Fig. 3), both multiple laminations and homogenous parts are thin and nondistinct. There are also thin sedimentary events that are significantly affected by bioturbation, although multiple laminations can still be observed (2-A, 18-A, 11-K, 4-B, 17-E, 9-D, 3-F, 3-B, and 3-C). All of these events we also classified as "Type I: Turbidites" since they show multiple laminations, implying multiple mass wasting events along basin slopes.

Some hazy, but still relatively darker levels, can be seen in the radiographic images (e.g., 9-B, 17-B, 2-C, and 18-B in Fig. 3), although they neither include multiple laminations nor foraminifera-free homogenous parts. We also classified these levels as sedimentary events, since their darker radiographic view implies a sudden influx of coarser hemipelagic sediment arrival at the coring location. We interpret them as either thin and singular turbidites or flood deposits that were dispersed within the background sediments by intense bioturbation. Hence, we classify them as "Type II: Turbidite or Flooding" events.

Type III events are characterized by their thickness, darker appearance in radiographic images (e.g., 17-C, 17-F, and 18-D in Fig. 3), and coarser grain-size compared to the background sediments, which is evident from their Sand (%) values (9-F, 11-F, 11-I, 11-M, 17-C, 17-F, and 18-D in Fig. 5). Unlike Type I events, Type III events are bioturbated, lacking any lamination, and containing biogenic remains. We consider three possible explanations regarding their origin. Firstly, it is possible that Type III events are turbidites that underwent complete bioturbation after deposition. However, considering that coarser sediments typically exhibit less vertical penetration of bioturbation (Wheatcroft, 1992), and given that Type III events are noticeably coarser than the background sediments, it is unlikely that these events underwent extensive bioturbation after deposition. Another possibility is that Type III events originated from hemipelagic sediments highly rich in biogenic content, hence their turbidites contain abundant bio-

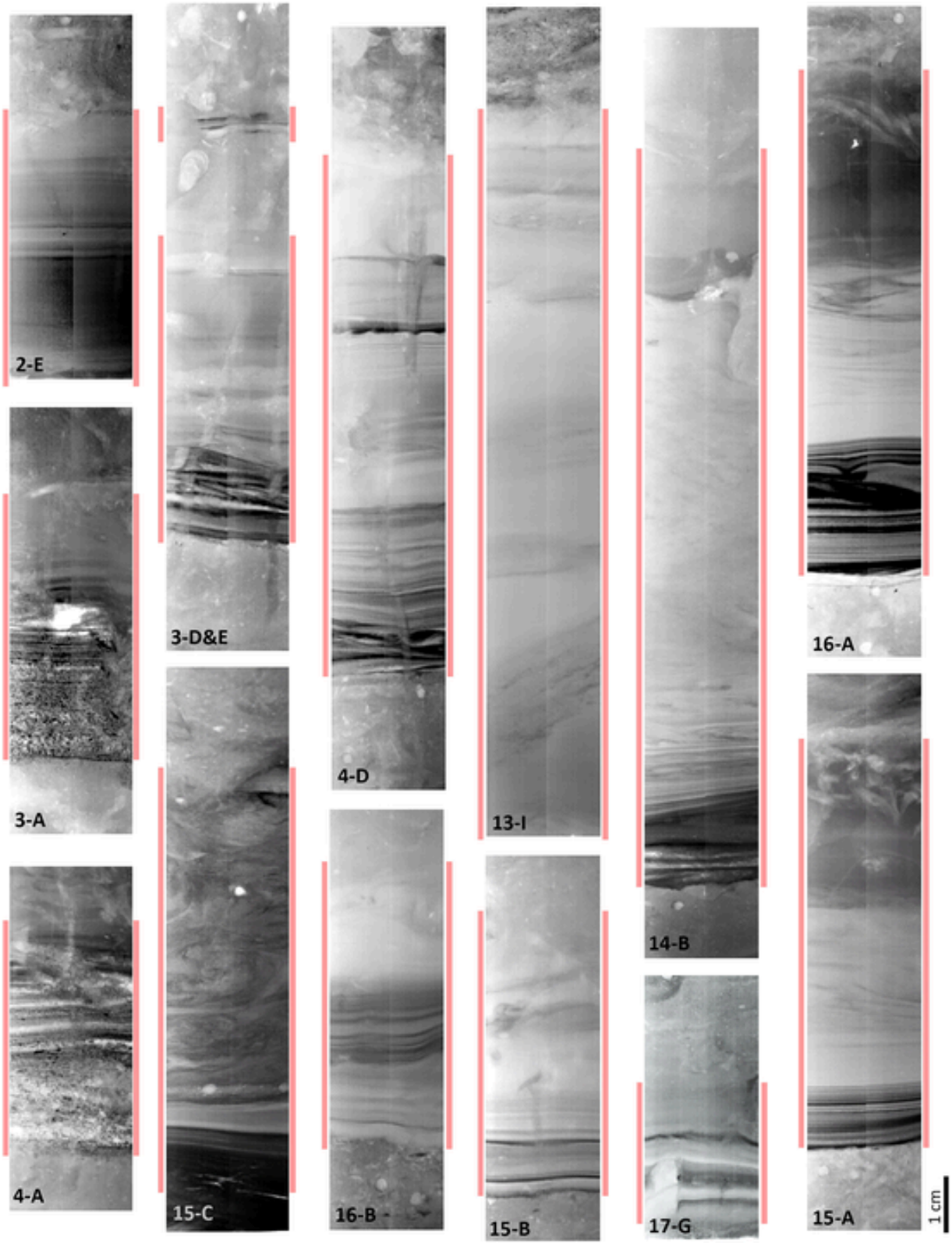

Fig. 2. U-channel radiographic images of prominent and well-preserved turbidites (Type I; red bars) in the sediments of the Gulf of Aqaba. Note the bioturbation and biogenic content (e.g., carbonaceous shells seen as whitish spots) in the background sedimentation. Event labeling is given in the lower left of each image.

genic remains as well (e.g., Van Daele et al., 2017; Polonia et al., 2023). However, if this was the case, we would expect to observe some evidence of multiple laminations or fining-upward grain-size trends in Type III events, which is not observed. The most plausible explanation for these events is that, during their deposition, there was sufficient time for organisms to dig and burrow, and for biogenic remains from the water column to be included into the sediments. Consequently, the deposition of Type III events was likely slower than that of Type I and Type II events. These events likely represent a series of successive flooding events that occurred over a period of several years or decades. We

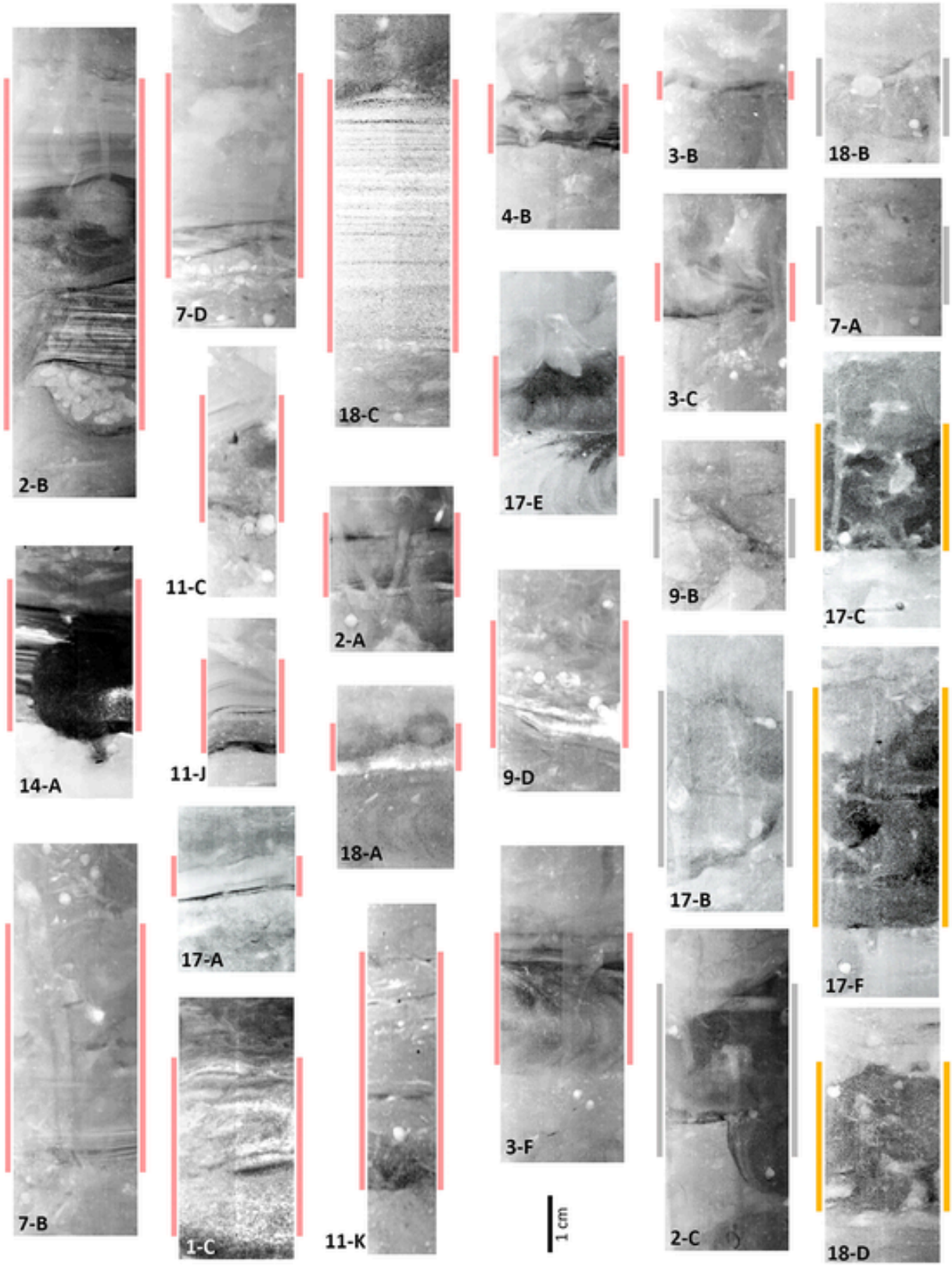

Fig. 3. U-channel radiographic images of different types of sedimentary events. Type I: Turbidites (red bars), Type II: Turbidite or Flooding (gray bars), and Type III: Thick Flooding Sequence (yellow bars).

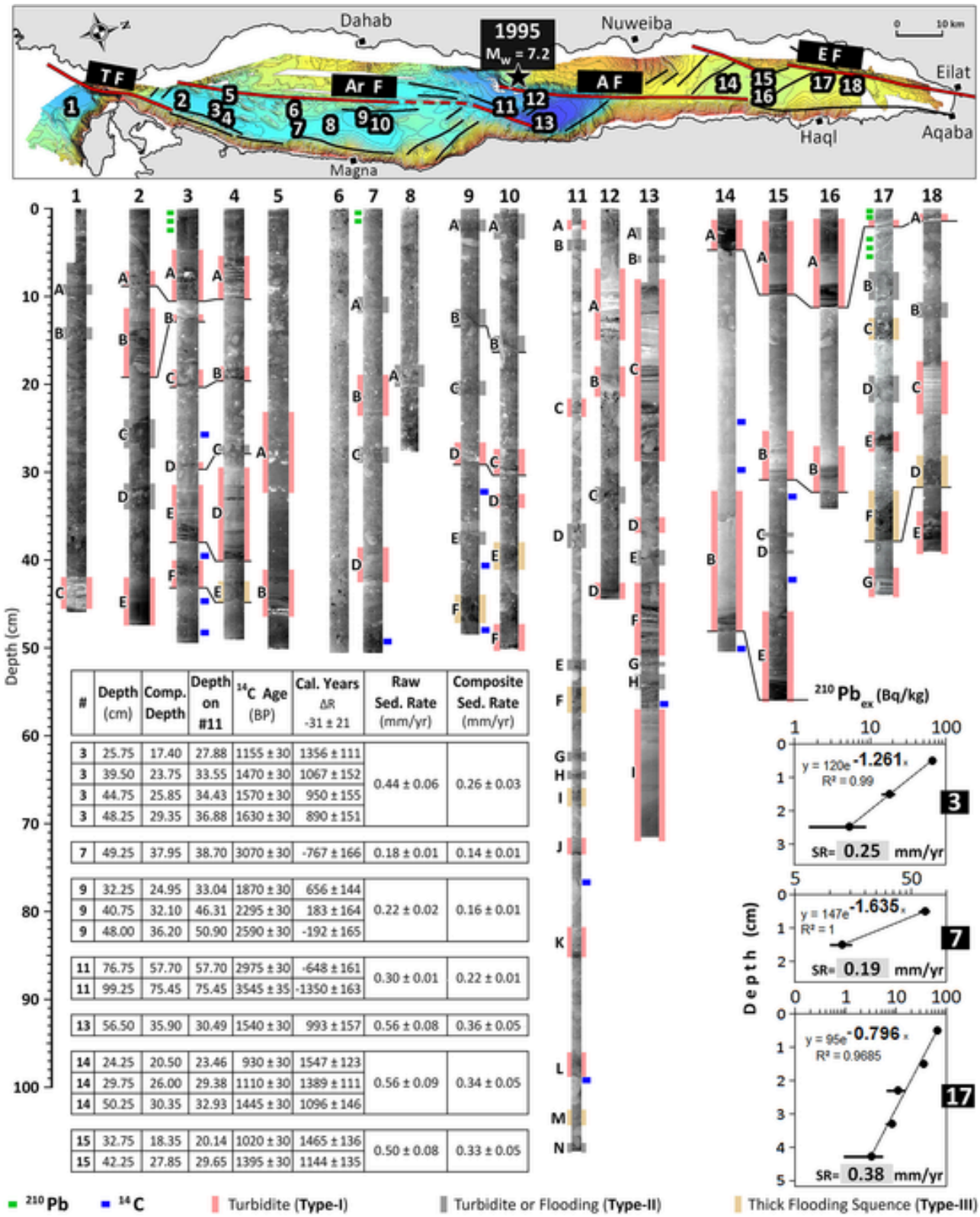

#	Depth (cm)	Comp. Depth	Depth on #11	^{14}C Age (BP)	Cal. Years ΔR -31 ± 21	Raw Sed. Rate (mm/yr)	Composite Sed. Rate (mm/yr)
3	25.75	17.40	27.88	1155 ± 30	1356 ± 111	0.44 ± 0.06	0.26 ± 0.03
3	39.50	23.75	33.55	1470 ± 30	1067 ± 152		
3	44.75	25.85	34.43	1570 ± 30	950 ± 155		
3	48.25	29.35	36.88	1630 ± 30	890 ± 151		
7	49.25	37.95	38.70	3070 ± 30	-767 ± 166	0.18 ± 0.01	0.14 ± 0.01
9	32.25	24.95	33.04	1870 ± 30	656 ± 144	0.22 ± 0.02	0.16 ± 0.01
9	40.75	32.10	46.31	2295 ± 30	183 ± 164		
9	48.00	36.20	50.90	2590 ± 30	-192 ± 165		
11	76.75	57.70	57.70	2975 ± 30	-648 ± 161	0.30 ± 0.01	0.22 ± 0.01
11	99.25	75.45	75.45	3545 ± 35	-1350 ± 163		
13	56.50	35.90	30.49	1540 ± 30	993 ± 157	0.56 ± 0.08	0.36 ± 0.05
14	24.25	20.50	23.46	930 ± 30	1547 ± 123	0.56 ± 0.09	0.34 ± 0.05
14	29.75	26.00	29.38	1110 ± 30	1389 ± 111		
14	50.25	30.35	32.93	1445 ± 30	1096 ± 146		
15	32.75	18.35	20.14	1020 ± 30	1465 ± 136	0.50 ± 0.08	0.33 ± 0.05
15	42.25	27.85	29.65	1395 ± 30	1144 ± 135		

Fig. 4. Sedimentary events detected in the radiographic images of the GA cores, labelled by letters and indicated by red, gray, and yellow vertical bars. Depths of ^{210}Pb and ^{14}C measurements are also shown by green and blue rectangles next to the images, respectively. In the table, raw and calibrated ^{14}C results are listed. The raw and composite depths, and the depths corresponding on core 11 (after stratigraphical correlation) for each ^{14}C sample are also given. In the lower right, results of $^{210}Pb_{ex}$ measurements on cores 3, 7, and 17 and the corresponding sedimentation rates (SR) are presented.

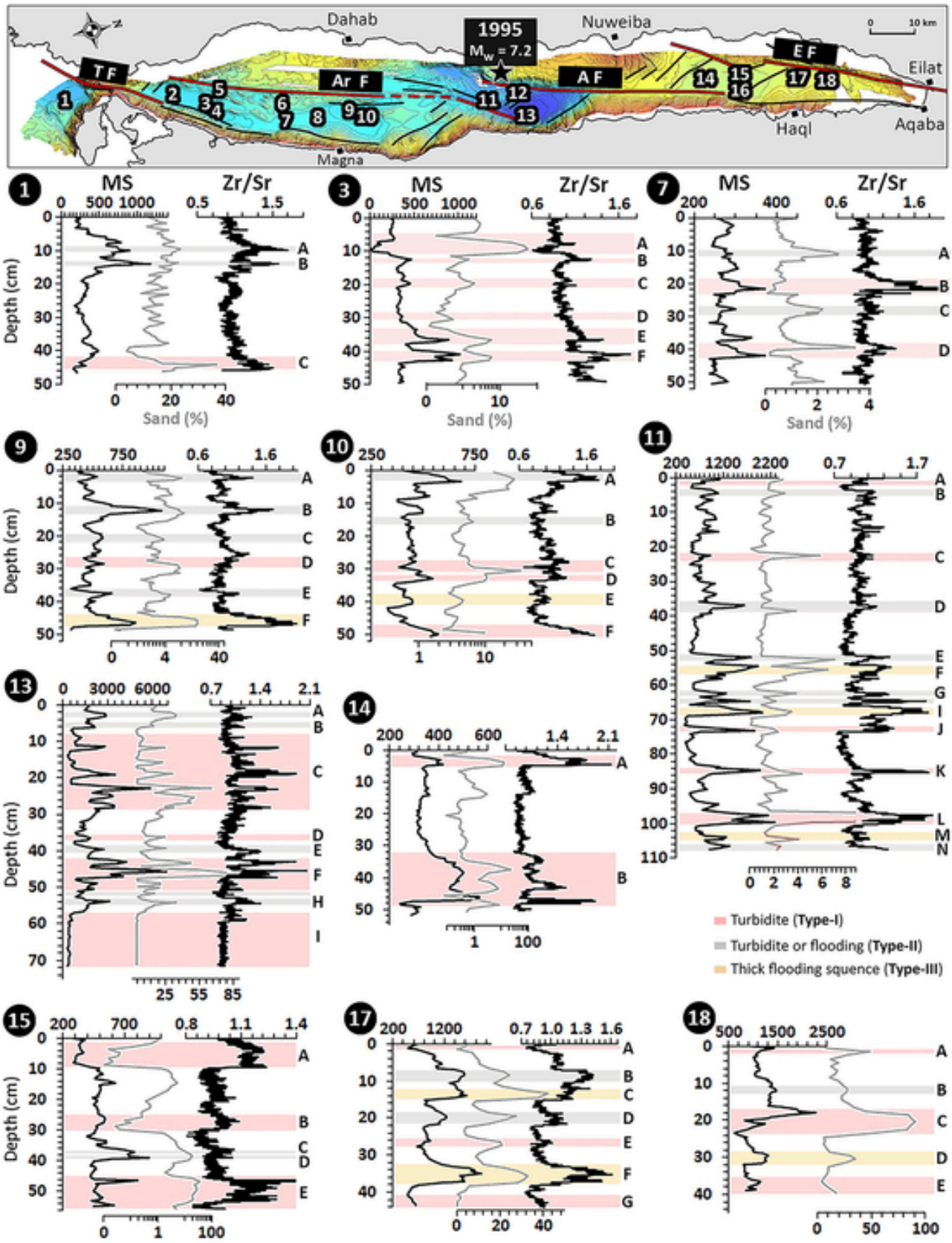

Fig. 5. Magnetic susceptibility (MS), sand content, and Zr/Sr profiles produced along selected cores (at least one core per basin) through the Gulf of Aqaba. Sedimentary events shown in Fig. 4 are also shown as horizontal bars in this figure. Event labeling and color code for different types of events are the same as in Fig. 4. See the Supplementary Material (E-SUPP 1) for detailed descriptions of sedimentary events for all of the cores.

classify these events as "Type III: Thick flooding sequence". For a more detailed classification of sedimentary events, please refer to the Supplementary Material (E-SUPP 1).

Fig. 4 shows radiographic images of all the 18 cores side-by-side along the gulf, together with the depths of ^{14}C and ^{210}Pb measurements and their results (Table in Fig. 4). The stratigraphic order of the dated samples confirms that our samples were collected in regular sedimentation sections and not in any anomalous sedimentary event. Radiocarbon results of 16 samples show that most of the cores include the sedimentary record for at least the last 1000 years.

We applied the "Constant Flux Constant Sedimentation Rate" model (Goldberg, 1963) on the $^{210}Pb_{ex}$ (excess lead) from the cores 3, 7, and 17, which yielded sedimentation rates of 0.25, 0.19, and 0.38 mm/yr for the top parts of these cores, respectively. It should be noted that event 17-A was excluded from the depth scale for the sediment rate calculation of core 17. Although the number of radionuclide samples collected from core 7 is insufficient to achieve a statistically meaningful sedimentation rate, the $^{210}Pb_{ex}$ results from cores 3 and 17 can be compared with the radiocarbon ages. For core 3, ^{14}C at the bottom of the core yields a bulk sediment rate of 0.44 mm/yr, which is inconsistent with the rate obtained by $^{210}Pb_{ex}$ for the same core (0.25 mm/yr). However, ^{14}C-based sediment-rate calculation by using composite depths, which are obtained by excluding the sedimentary events, yields a composite sediment rate of 0.26 mm/yr that is consistent with the $^{210}Pb_{ex}$ sediment rate. Similarly, ^{14}C-based bulk rates for cores 14 and 15 (0.56 and 0.50 mm/yr, respectively) in Eilat Deep are much higher than the $^{210}Pb_{ex}$-based sediment rate obtained for core 17 (0.38 mm/yr) from the same basin. However, once corrected by removing the event layers, the ^{14}C-based composite sediment rates for cores 14 and 15 (0.34 and 0.33 mm/yr, respectively) are rather consistent with the 0.38 mm/yr derived from the $^{210}Pb_{ex}$ measurements. Thus, these two comparisons confirm the importance of determining both the bottom and top boundaries of sedimentary events to properly exclude them from the sequences and hence to construct reliable sediment chronology.

In order to cross-check the existence and extent of the sedimentary events in the cores, we compared our visual inspections of the radiographic images to magnetic susceptibility, grain-size (only sand content) and μ-XRF measurements (Fig. 5). For these analyses, at least one core per basin was selected. During floods or mass wasting events, coarser sediments originating from the shallower parts of the basin or from drainages onshore are expected to reach bottom of the basins. Thus, sand content in the event deposits is expected to increase compared to the background sedimentation. Deep marine sediments are normally a mixture of terrigenous clastics (mainly aluminosilicate minerals) and bio/chemical carbonates produced in the water column. However, there is almost no bio/chemical carbonate input during the almost instantaneous deposition of turbidite or flood deposits, which makes them richer in terrigenous clastics compared to the background sediments. Since aluminosilicates have higher magnetic susceptibility values than carbonates (Nowaczyk, 2001), turbidite and flood deposits should show as anomalies along the magnetic susceptibility profiles of the cores. Similarly, Zr/Sr profiles, where Zr and Sr represent aluminosilicates and foraminiferal calcite, respectively (Rothwell et al., 2006; Croudace and Rothwell, 2015), should show anomalies at turbidite and flood levels.

Among the 67 events shown in Fig. 5, significant magnetic susceptibility anomalies are observed for 51 of them. While 11 events (1-C, 3-D, 7-A, 9-C, 10-B, 10-C, 13-I, 15-C, 17-E, 17-G, and 18-B) show almost no magnetic susceptibility anomalies, only three events (3-A, 15-A, and 17-A) have clearly lower magnetic susceptibility values than the background sediments. Sand fraction profiles show distinct anomalies for 57 events out of 67. On the other hand, events 7-B, 15-A, 15-B, and 17-A have lower sand content compared to the background sediments. No sand anomalies are observed for four events (1-A, 1-B, 13-I, and 17-G). Since no μ-XRF scanning was done for core 18, 62 events can be tested for Zr/Sr anomalies. Among these, 49 events show higher and only two events (3-A and 17-A) lower Zr/Sr anomalies. Nine events (3-C, 3-D, 7-A, 9-C, 10-B, 11-A, 11-B, 13-D, and 13-I) show no Zr/Sr anomalies. Accordingly, from the data presented in Fig. 5, we note that magnetic susceptibility, sand content, and Zr/Sr profiles are successful in detecting sedimentary events observed on the radiographic images at rates of 81%, 91%, and 79%, respectively. Although Type I and Type III events are already evident in the radiographic images, some Type II events are unclear in the images (e.g., 7-A in Fig. 3). Magnetic susceptibility, sand content, and Zr/Sr profiles, together with the radiographic images, were therefore particularly useful to confirm/detect the thickness of Type II events, so that all sedimentary events were successfully excluded from the sequences covered by the cores to achieve reliable stratigraphical correlations and sediment chronology.

4.2. Chemostratigraphical correlation and sediment chronology

Coevality of turbidites at different locations and even in different basins should be tested to achieve successful submarine paleoseismological records (e.g., Goldfinger, 2011), which can be achieved by careful high-resolution stratigraphical correlations. In Fig. 4, some of the sedimentary events can be visually correlated between cores collected from the same basin according to their stratigraphical order, e.g., between the cores 2, 3, and 4 in Tiran basin, cores 9 and 10 in Dakar basin, and cores 14, 15, 16, 17 and 18 in Eilat basin. However, visual observations are not reliable enough for inter-basin correlations between the cores as one cannot assume that the number of turbidites in different basins is the same. Stratigraphical correlations between cores can be achieved by using data reflecting geophysical and geochemical properties of sediments, which may include magnetic susceptibility, bulk density, grain-size distribution, computed tomography (CT) image analysis, micro-XRF data and paleomagnetic secular variation (PSV) records (Patton et al., 2013; Drab et al., 2015; Ikehara et al., 2016; Goldfinger et al., 2017; Usami et al., 2018). In our study, geophysical and geochemical properties of sediments were evaluated by magnetic susceptibility and grain-size measurements (Sand percent), and micro-XRF scanning, of which resolutions were 5 mm, 10 mm and 0.5 mm, respectively. Micro-XRF data, which has significantly higher resolution than the other proxies, was preferred for core correlation. Reliable chemostratigraphical correlations over large distances, like in our case where the cores are distributed along the ~180-km-long gulf, can only be successfully achieved by using a sedimentary geochemical proxy recording regional environmental conditions effective for the entire gulf. It is known that Sr/Ca ratios of planktonic foraminifera have a strong positive correlation with sea-surface temperature (e.g., Cléroux et al., 2008). Since the sediments of the Gulf of Aqaba are rich in planktonic foraminifera, and by assuming that the surface seawater temperatures would synchronously change over the entire gulf, we used Sr/Ca ratio profiles to correlate the cores in this study.

We intentionally collected core 11, the longest core in this study, from a ridge just to the south of the Aragonese Deep, rather than from the depocenter of the basin (Fig. 1d), so that it would dominantly reflect the background sedimentation recording the climatic conditions rather than being dominated by turbidites. To achieve reliable stratigraphical correlations, sedimentary events should be excluded from the sequences, and correlations should be done on composite profiles representing background sedimentation (Arnaud et al., 2002; Schwab et al., 2009; Avşar et al., 2015; Moernaut et al., 2017). After excluding the sedimentary events, we correlated the composite Sr/Ca profiles of all the cores to the composite Sr/Ca profile of core 11 (Fig. 6). As the sedimentation rates are different between basins, this resulted in squeezing or stretching of the core records. This calibration was done using 5 to 8 characteristic reference levels that can be recognized in all the cores, which we used as tie-points to ensure consistency between the cores through the calibration process. (Gray lines in Fig. 6). Detailed explana-

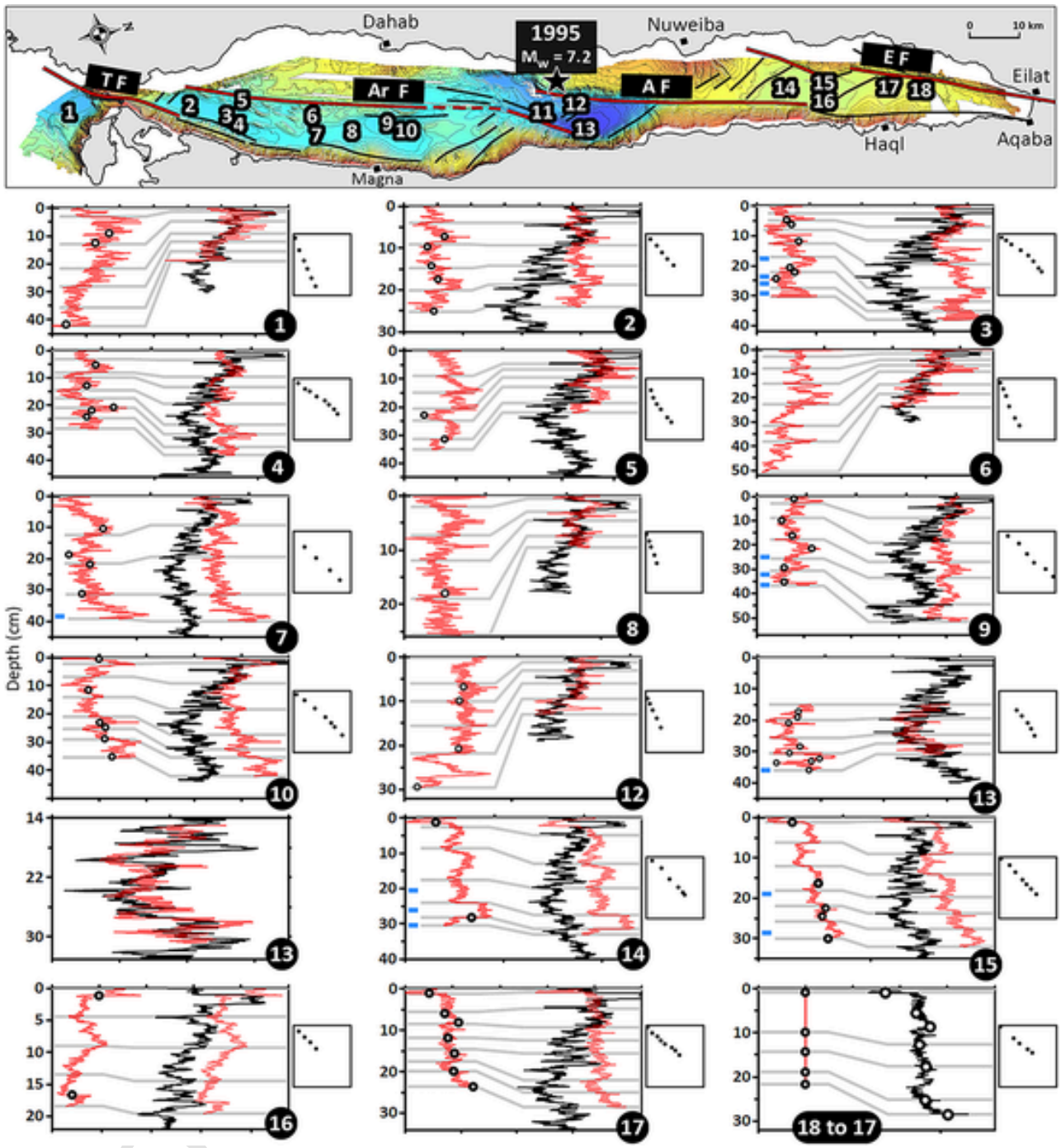

Fig. 6. Chemostratigraphical correlation of composite Sr/Ca ratio profiles (event-free) of each core (red curves) to core 11 (black curves). Depths of sedimentary events and radiocarbon dates are shown as dots and blue rectangles, respectively. Bi-plots next to each graph show the original composite depths (y-axes) versus the modified depths on core 11 (x-axes) of the tie-lines (gray lines). Details of the chemostratigraphical correlation procedure are presented in the Supplementary Material (E-SUPP 2).

tion of the procedure for the removal of the sedimentary events and chemo-stratigraphical correlation can be found in Supplementary Material (E-SUPP 2). The original and modified depths of these tie-points are also presented as bi-plots next to each correlation plot in Fig. 6. Almost linear and smooth appearances of these bi-plots confirm that depth modifications did not result in abnormal sedimentation rates.

For five cores (1, 6, 8, 12, and 13), the chemostratigraphical correlations result in almost perfect overlaps with core 11. For most of the other cores, although exact overlaps are not achieved, similarities between general trends and fluctuations along the cores are still within the range of uncertainties and thus are deemed acceptable. The discrepancies are probably due to the semi-quantitative nature of ITRAX μ-XRF scanning data or local differences in sedimentation. In addition, cores 11 and 13 were collected by a piston corer, which sometimes causes a disturbance and sediment loss close to the water/sediment interface. However, a good correlation between cores 11 and 12, which was taken by a multicorer ensuring undisturbed recovery of water/sediment interface, confirms that there was no sediment loss at the top of core 11. On the other hand, correlation between cores 11 and 13 shows that approximately 15 cm-thick sediment was lost at the top of core 13 during cor-

ing operation. A close-up view of the correlation between cores 13 and 11 is also provided in Fig. 6. Correlation between cores 17 and 18 is based on the stratigraphical order of the events since no μ-XRF data is available for core 18.

The raw ^{14}C dates listed in Fig. 4 were included in the OxCal P_Sequence code (E-SUPP 3) with respect to their modified depths obtained by the chemostratigraphical correlations, as if all the radiocarbon samples came from core 11. The k value for the P_Sequence function was selected as 3, which is generally used for deep sea environments where hemipelagic sedimentation can be assumed rather constant (e.g., Polonia et al., 2023). Although the dates show a reasonable trend along core 11 (Fig. 7), two dates, the one from the bottom of core 7 (7–38.70) and the youngest date from core 9 (9–33.04), are clearly older than the general trend. Hence, we interpret them as reworked material and did not use them in the P_Sequence code. The resulting age-depth model, which is presented with 68% and 95% confidence intervals in Fig. 7, yields approximate sedimentation rates of 0.35, 0.16 and 0.22 mm/yr for the intervals of 0–32 cm, 32–55 cm and 55–80.5 cm, respectively. All of the sedimentary events projected on core 11 are also plotted with respect to depth in Fig.7, and are included in the P_Sequence code (E-SUPP 3), so that probability density functions (PDFs) for each event detected in Gulf of Aqaba can be calculated.

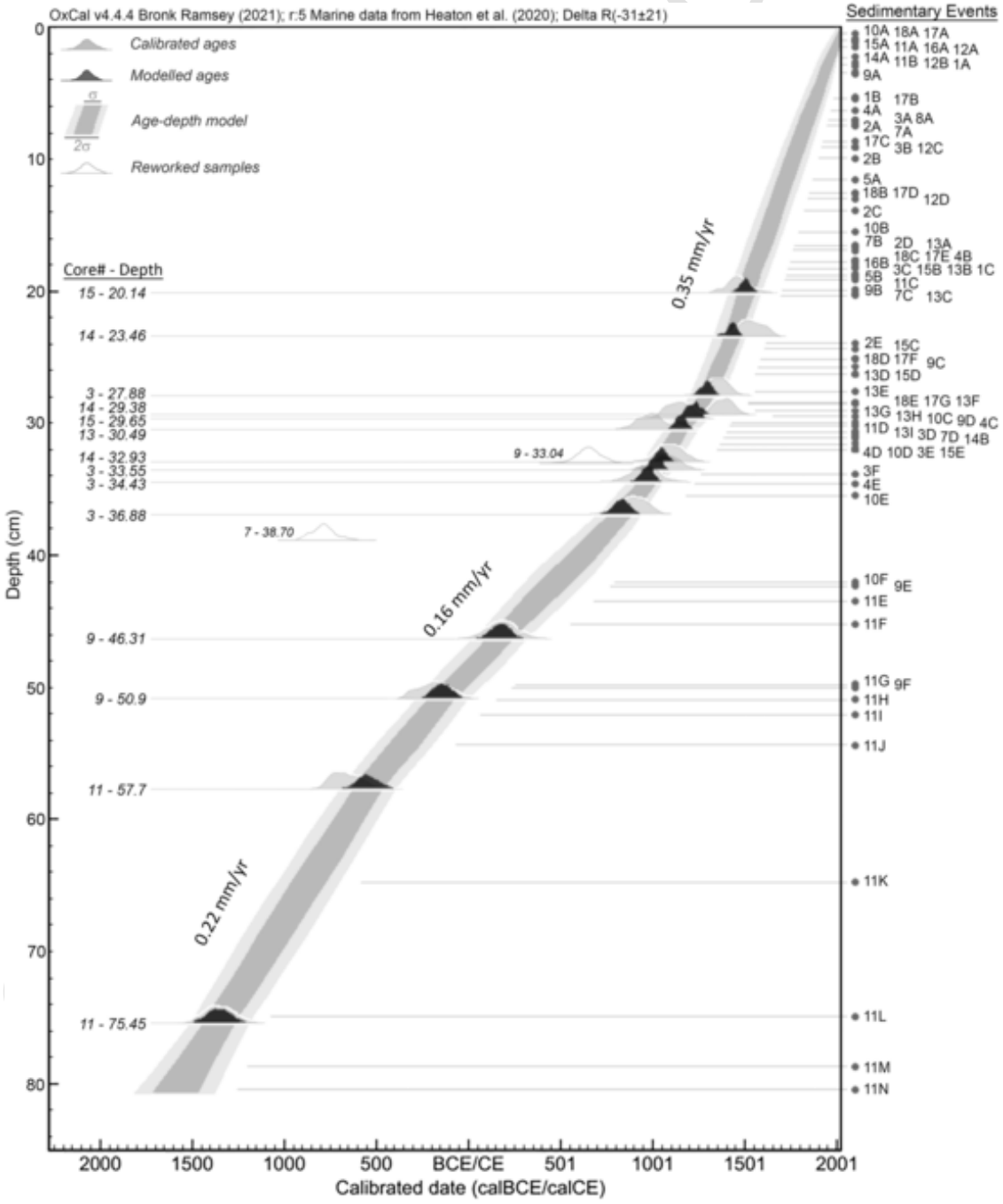

Fig. 7. Calibrated radiocarbon dates, and the age-depth model determined by OxCal P_Sequence function. Two reworked samples (9–33.04 and 7–38.70) were not included in the P_Sequence code, which can be found in the Supplementary Material (E-SUPP 3). The list and depths of all sedimentary events are also shown.

5. Discussion

PDFs of Type I and Type II events in the cores through the gulf are plotted with respect to calendar dates in Fig. 8, which were obtained according to the age-depth relation presented in Fig. 7. The probability density values for Type II events were multiplied by 0.5 since they may also be floods. Type III events, which are most probably not related to earthquakes, were not included in this plot. In Fig. 8, the plot of summed PDFs is also presented in order to statistically express the spatial extent and coevality of turbidites in the gulf; i.e., multiple coeval turbidites should be seen as distinct anomalies on the summed PDFs profile. Several sedimentary events appear to be coherent for several cores, including cores located in different basins. Hence, they are seen as anomalies in the summed PDFs profile (e.g., around late 10th, 16th and 20th centuries CE), and we interpret these events as the signature of past earthquakes that triggered turbidites (Type I or II) in the GA.

The turbidites dated to the late 20th century are unambiguously seen as Type I events at the tops of cores in Aragonese and Eilat Deeps (Cores 11, 12, 14, 15, 16, 17, and 18) and as Type II event in Dakar Deep (Core 10). They constitute a perfect benchmark of our sedimentary system as they are almost certainly the sedimentary traces of the 1995 Nuweiba (M_w 7.2) earthquake, the most recent major earthquake in the Gulf of Aqaba. Given that the Aragonese Fault, and probably partially the Eilat Fault as well, were the source faults for the 1995 Nuweiba earthquake and that the earthquake rupture propagated northward (Baer et al., 2008; Hofstetter, 2003; Klinger et al., 1999; Shamir et al., 2003; Ribot et al., 2021), it is not surprising that turbidites (Type I events) from this earthquake are not found in cores from the southern part of the gulf (i.e., cores 1 to 10). Despite the proximity to the epicenter of the 1995 earthquake, no turbidite associated with this event is visible in core 13 due to sediment loss at the top of that core (Fig. 6).

Among older turbidites, two events stand out and are recognized almost in every core, one in about the early 12th century CE and one in about the late 16th century CE. Starting from the oldest turbidites, one series of turbidites are clearly visible as Type I events in all cores (except core 11), which are long enough to cover at least the last millennium (Fig. 8). Since core 11 is not a turbidite-targeting core, and it was collected from a ridge rather than from a depocenter, it can be expected to see only limited evidence for turbidites in this core. The significant anomaly on the summed PDFs profile, near the beginning of the 12th century CE is most probably associated with the only major earthquake known in the region during that period: the CE 1068 earthquake. The temporal discrepancies observed for dates of turbidites in some cores are most probably related to the difficulties of the inter-core chemostratigraphical correlations due to intense bioturbation in the sediments of the Gulf of Aqaba that can lead to small time shifts when it comes to estimate exact age of specific core sections. The 18 March

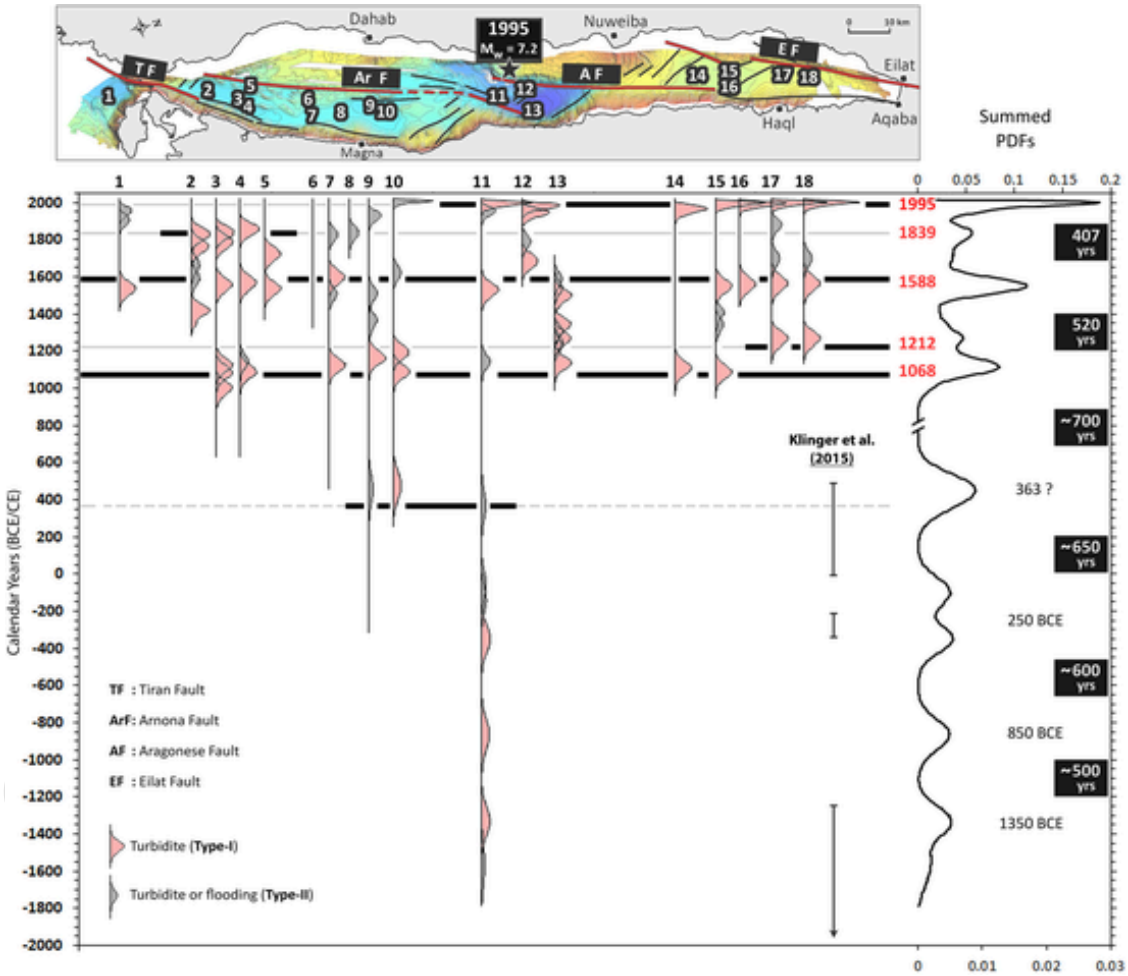

Fig. 8. Plot of Probability Distribution Functions (PDFs) of Type I and Type II events along the Gulf of Aqaba. Horizontal black lines mark the dates of historical earthquakes in the region. Major earthquakes that triggered extensive turbidites all along the gulf are seen as major anomalies on the summed PDFs profile. The scale of x-axis changes around CE 800. Time windows for the prehistorical surface rupturing events at the Qatar trenching site (x in Fig. 1, Klinger et al., 2015) are also shown. Note the recurrence intervals varying between 400 and 700 years and also the absence of extensive coeval turbidites in the southern half of the gulf since CE 1588.

1068 Aqaba-Hijaz earthquake was reported to have devastating effects in many locations from the city of Aila (Eilat) to Medina and Cairo (Ambraseys, 2009). Presence of seismo-turbidites all along the gulf in addition to evidence found at the onshore paleoseismic sites north of the Gulf (Amit et al., 1999, 2002; Zilberman et al., 2005; Klinger et al., 2015; Kanari et al., 2020) indicate that the CE 1068 earthquake was a major earthquake in the region that ruptured the Eilat, Aragonese, Arnona and probably Tiran faults together, in addition to the southernmost part of the Wadi Arabah Fault near the gulf. Hence, the total rupture length of this earthquake could have been at least ~200 km.

Similar as for the CE 1068 event, numerous coeval turbidites along the Gulf of Aqaba are represented by the anomaly on the summed PDFs profile about late 16th century CE, which is consistent with the well-documented earthquake of 4 January 1588 (Ambraseys, 2009). Majority of them are of Type I events, except the ones in core 2 in Tiran Deep, and in cores 9 and 10 in Dakar Deep, which are of Type II. The absence of turbidites in core 6 can be explained by the fact that this core was collected from a small and isolated basin (Fig. 1e). Indeed, this basin is isolated from turbidity flows that would come from the main slopes of the gulf, and its relatively smaller slopes may not be sensitive to earthquake shaking as much as the larger main slopes of the gulf. An absence of a turbidite in core 14 is more difficult to explain. One possible explanation could be the sediment clearance on the slopes and the banks of the submarine channels during the preceding earthquake, i.e., in CE 1068, leaving nothing to be wasted during the CE 1588 earthquake. Furthermore, another possibility is that the turbidity flows due to 1588 earthquake might have bypassed the location of core 14 (Goldfinger et al., 2017). Apart from turbidite absence in these three cores, it seems that the CE 1588 earthquake triggered seismo-turbidites along the entire gulf. This earthquake is also known as a devastating event in the historical records, affecting many places from the cities of Eilat and Aqaba at the northern end of the gulf to Cairo in Egypt (Ambraseys, 2009). A second event is also reported in the historical chronicles that happened on 7 April 1588, which was felt in Cairo and in the northern Red Sea. Although it cannot be ruled out that this second event was completely independent of the event in January 1588, it could be an aftershock of the former event (Ambraseys, 2009), triggering additional turbidites for example along the Tiran fault section. Klinger et al. (2015) report no surface rupturing evidence for the CE 1588 earthquake at the Qatar trench site (x in Fig. 1b). On the other hand, Kanari et al. (2020) report both rupturing and paleoliquefaction evidences that could be related to this earthquake in the Eilat Sabkha (t in Fig. 1b). Hence, based on our seismo-turbidite observations, it appears that the CE 1588 earthquake likely also ruptured the entire fault system in the Gulf of Aqaba. Unlike in CE 1068, however, the 1588 rupture does not seem to have propagated inland beyond the northern end of the gulf. In the south, based on turbidites we can trace the rupture to the south of the Tiran Strait and it may have ruptured even further to the south.

Some additional sequences of turbidites are found in our record, although they are not as extensive as the sequences associated respectively to the CE 1068 and CE 1588 earthquakes. According to the historical records, the CE 1212 earthquake caused widespread damage in an extensive area from Al-Shaubak and Al-Karak in the north (ca. 150 km north of Eilat and Aqaba cities) to the St Catherine Monastery in the south (ca. 50 km east of Dahab) (Ambraseys, 2009). Although Klinger et al. (2015) reported evidence of surface rupturing along the southern Wadi Arabah Fault (Qatar Site, x in Fig.1b) that could be related to the CE 1212 earthquake, the trenching studies closer to the gulf (Zilberman et al., 2005; Kanari et al., 2020; y and t in Fig. 1b, respectively) claim that the CE 1212 earthquake was likely generated by a secondary fault on the eastern edge of the Eilat depression, rather than by the Wadi Arabah Fault. The probable turbidites of the CE 1212 earthquake are only seen in cores 17 and 18 from the northernmost part of the gulf (Fig. 8). Thus, it appears as a minor anomaly in the summed PDFs profile. The turbidite in core 18 is thicker and better preserved with its laminated internal structure. Furthermore, there are no turbidites in cores 14 and 15 around 1200s. Given the absence of consistently coeval turbidites through the gulf that are dated to the beginning of the 13th century (except the one in core 13), and only two turbidites in the northernmost cores (17 and 18), we conclude that the CE 1212 earthquake was likely significantly smaller than the CE 1068 and CE 1588 events. The exact location of this event north of the gulf remains uncertain, but it might have caused a discontinuous rupture on fault segments of the Wadi Arabah Fault system.

Prominent turbidites with well-preserved internal structures are seen around the mid-19th century CE in cores 2, 3 and 4. No turbidites were found around this period in the neighboring cores, except Type II events in cores 1, 7, and 8. The summed PDFs profile has a minor anomaly due to these turbidites that are limited to the most southern part of the gulf. These turbidites are probably related to the CE 1839 earthquake, which is described in the historical records as causing minor damage on the walls of St Catherine Monastery (Ambraseys, 2009). Furthermore, Purkis et al. (2022) reported an incipient submarine landslide on the southeastern slopes of Tiran Deep that failed within the last 500 years, plausibly triggered by the CE 1839 earthquake. Given that the turbidites in cores 2, 3, and 4 are limited only in Tiran Deep, it is likely that the CE 1839 earthquake only partially ruptured either the Tiran or Arnona fault, or activated one of the secondary faults in the southernmost part of the gulf. Except for the ones related to the CE 1839 earthquake, the absence of distinct coeval turbidites in cores 1 to 10 (southern half of the gulf) since CE 1588 implies that most of the Tiran and Arnona faults has not ruptured since then.

While the cores provide a detailed record for the past millennium, only a few cores provide information for earlier periods. Around the middle 5th century CE, there are implications of coeval turbidites in cores 9, 10, and 11 in Dakar and Aragonese basins. Klinger et al. (2015) report evidence of surface rupturing at the Qatar trenching site on the Wadi Arabah Fault between 9 BCE and CE 492 (Fig. 8), which they attribute to the CE 363 earthquake that affected significantly the southern part of the Dead Sea Fault (Thomas et al., 2007; Ambraseys, 2009). However, this event could not be found north of the Qatar site (Lefevre et al., 2018). Hence, the turbidites around the middle 5th century CE could be due to a large earthquake rupturing several faults in the gulf, in addition to a 50 km long on-shore fault section. In core 11, three more Type I events, which can be other earthquakes in the gulf, are dated to ca. 250, 850 and 1350 BCE. The one around 250 BCE temporally correlates well with the event between 338 and 213 BCE, detected by Klinger et al. (2015) (Fig. 8). Although Klinger et al. (2015) do not report any event around 850 BCE, they report two events occurred during the period 2797–1245 BCE, which also coincide with the date of the turbidite ca. in 1350 BCE.

From the oldest turbidite to the youngest in 1995, the recurrence intervals for major earthquakes in the gulf seem to vary between 400 and 700 years (Fig. 8), with a mean value of 560 years. According to the paleoseismic trenching studies conducted in the north of the Gulf of Aqaba region, the Dead Sea Fault is characterized by earthquake clusters lasting 100–200 years, followed by seismic quiescence periods of 350–400 years (Klinger et al., 2015; Lefevre et al., 2018). On the other hand, Lefevre et al. (2018) have proposed that recurrence intervals for events should be longer due to partial stress partitioning between offshore and on-land fault segments, which is consistent with the 560 years recurrence interval found in the Gulf of Aqaba. In addition, the left-lateral relative plate motion between the Sinai and Arabian plates at this latitude is almost 5 mm/year (Castro-Perdomo et al., 2022; Viltres et al., 2022), which yields about 2 to 3.5 m fault slip deficit in a 400–700 year period, corresponding to an expected surface rupture length of 100–180 km (Wells and Coppersmith, 1994), which would be consistent with multi-segment rupturing events in the gulf. However, recent studies based on InSAR and GNSS observations (Li et al., 2021;

Castro-Perdomo et al., 2022) report fault-locking depths that become shallower towards the south and possibility of partial fault creep along the southernmost fault strands of the gulf. Still, our results indicate that the entire Gulf of Aqaba fault system was activated in the 1068 and 1588 earthquakes and probably during the previous major earthquakes. This implies that the southern gulf can be regarded as being close to the end of the earthquake cycle as it has not ruptured in a major earthquake for more than 400 years.

6. Conclusions

Based on ITRAX μ-XRF scanning, radiographic imaging, magnetic susceptibility measurements and grain-size measurements, we detected a total of 86 sedimentary events in 18 sediment cores collected from the Gulf of Aqaba. Of these events, 46 were classified as distinct turbidites, 9 events described as thick flooding sequences due to high precipitation periods lasting probably several decades, and the remaining 31 less distinct events as turbidites or floods. Careful chemostratigraphical intercore correlations and radiometric dating of these events provide a robust submarine paleoseismic record for the last millennium. The results show that the historical earthquakes in 1068 and CE 1588 were major characteristic earthquakes in the gulf that probably ruptured all the main faults (Tiran, Arnona, Aragonese and Eilat faults) in the gulf. On the other hand, the historical earthquakes of 1839 and CE 1212 were smaller and triggered only local turbidites in the southernmost and northernmost parts of the gulf, respectively. Information on older major events, together with the 1068 and CE 1588 earthquakes, suggests a recurrence interval of 400–700 years (average = 560 years), indicating that the southern gulf is a ripe for a major earthquake.

CRediT authorship contribution statement

Zeynep Bektaş: Writing – original draft, Visualization, Validation, Software, Methodology, Investigation, Formal analysis, Data curation. **Ulaş Avşar:** Writing – review & editing, Writing – original draft, Visualization, Validation, Supervision, Software, Resources, Project administration, Methodology, Investigation, Funding acquisition, Formal analysis, Data curation, Conceptualization. **Matthieu Ribot:** Writing – review & editing, Methodology, Data curation. **Yann Klinger:** Writing – review & editing, Supervision, Project administration, Methodology, Investigation, Funding acquisition, Data curation, Conceptualization. **Sigurjón Jónsson:** Writing – review & editing, Validation, Supervision, Resources, Project administration, Methodology, Investigation, Funding acquisition, Formal analysis, Data curation, Conceptualization.

Declaration of competing interest

The authors declare that they have no known competing financial interests or personal relationships that could have appeared to influence the work reported in this paper.

Data availability

Data will be made available on request.

Acknowledgment

The authors thank two anonymous reviewers for their useful suggestions that improved this manuscript. The authors also thank Rémi Matrau, Francis Mallon and Brian Hession, and the crew on R/V Thuwal for their work during the coring campaign (May–June 2018). This research was conducted within the scope of the "Interdisciplinary Earthquake Hazard Research in Gulf of Aqaba and Strait of Tiran – GAST" project (ORS-2016-CRG5–3027–03), which was funded by the King Abdullah University of Science and Technology (KAUST).

Supplementary materials

Supplementary material associated with this article can be found, in the online version, at doi:10.1016/j.epsl.2024.118595.

References

Ambraseys, N., 2009. Earthquakes in the Mediterranean and Middle East: A multidisciplinary Study of Seismicity Up to 1900, Cambridge University Press, Cambridge, p. 968. p.
Amit, R., Zilberman, E., Enzel, Y., Porat, N., 2002. Paleoseismic evidence for time dependency of seismic response on a fault system in the southern Arava Valley, Dead Sea Rift, Israel. Geol. Soc. Am. Bull. 114 (2), 192–206.
Amit, R., Zilberman, E., Porat, N., Enzel, Y., 1999. Relief inversion in the Avrona Playa as evidence of large-magnitude historical earthquakes, Southern Arava Valley, Dead Sea Rift. Quat. Res. 52 (1), 76–91.
Arnaud, F., Lignier, V., Revel, M., Desmet, M., Pourchet, M., Beck, C., Charlet, F., Trentesaux, A., Tribovillard, N., 2002. Flood and earthquake disturbance of ^{210}Pb geochronology (Lake Anterne, North French Alps). Terra Nova 14, 225–232.
Avşar, U., 2013. Lacustrine Paleoseismic Records from the North Anatolian Fault, Turkey. Doctoral dissertation. Ghent University, p. 209.
Avşar, U., Hubert-Ferrari, A., Batist, M.D., Fagel, N., 2014. A 3400 year lacustrine paleoseismic record from the North Anatolian Fault, Turkey: implications for bimodal recurrence behavior. Geophys. Res. Lett. 41 (2), 377–384.
Avşar, U., Hubert-Ferrari, A., Batist, M.D., Schmidt, S., Fagel, N., 2015. Sedimentary records of past earthquakes in Boraboy Lake during the last ca 600 years (North Anatolian Fault, Turkey). Paleogeogr., Palaeoclimatol., Palaeoecol. 433, 1–9.
Avşar, U., Jónsson, S., Avşar, Ö., Schmidt, S., 2016. Earthquake-induced soft-sediment deformations and seismically amplified erosion rates recorded in varved sediments of Köyceğiz Lake (SW Turkey). J. Geophys. Res.: Solid Earth 121 (6), 4767–4779.
Baer, G., Funning, G.J., Shamir, G., Wright, T.J., 2008. The 1995 November 22, Mw 7.2 Gulf of Elat earthquake cycle revisited. Geophys. J. Int. 175 (3), 1040–1054.
Ben-Avraham, Z., Almagar, G., Garfunkel, Z., 1979. Sediments and structure of the Gulf of Elat (Aqaba)–Northern Red Sea. Sediment. Geol. 23, 239–267.
Ben-Avraham, Z., Garfunkel, Z., Lazar, M., 2008. Geology and evolution of the southern Dead Sea Fault with emphasis on subsurface structure. Annu. Rev. Earth Planet Sci. 36 (1), 357–387.
Brady, H.B., 1877. Supplementary note on the foraminifera of the chalk(?) of the new Britain group. Geol. Magazine, new ser. 4, 534–536.
Bronk Ramsey, C., 2001. Development of the radiocarbon calibration program OxCal. Radiocarbon.Radiocarbon. 43 (2A), 355–363.
Bronk Ramsey, C., 2008. Deposition models for chronological records. Quat. Sci. Rev. 27, 42–60. https://doi.org/10.1016/j.quascirev.2007.01.019.
Castro-Perdomo, N., Viltres, R., Masson, F., Klinger, Y., Liu, S., Dhahry, M., Ulrich, P., Bernard, J.D., Matrau, R., Alothman, A., Zahran, H., Reilinger, R., Mai, P.M., Jónsson, S, 2022. Interseismic deformation in the Gulf of Aqaba from GPS measurements. Geophys. J. Int. 228 (1), 477–492.
Cléroux, C., Cortijo, E., Anand, P., Labeyrie, L., Bassinot, F., Caillon, N., Duplessy, J.C., 2008. Mg/Ca and Sr/Ca ratios in planktonic foraminifera: proxies for upper water column temperature reconstruction. Paleoceanography 23, Pa3214. https://doi.org/10.1029/2007pa001505.
Croudace, I.W., Rothwell, R.G, 2015. Micro-XRF Studies of Sediment Cores: Applications of a Non-Destructive Tool for the Environmental Sciences, Vol. 17. Springer, Dordrecht, Netherlands. 656 p.
Drab, L., Hubert-Ferrari, A., Schmidt, S., Martinez, P., Carlut, J., El Ouahabi, M., 2015. Submarine earthquake history of the Çınarcık segment of the North Anatolian Fault in the Marmara Sea, Turkey. Bull. Seismol. Soc. Am. 105 (2A), 622–645.
Fanetti, D., Anselmetti, F.S., Chapron, E., Sturm, M., Vezzoli, L., 2008. Megaturbidite deposits in the Holocene basin fill of Lake Como (southern Alps, Italy). Palaeogeogr. Palaeoclimatol. Palaeoecol. 259, 323–340.
Felis, T., Lohmann, G., Kuhnert, H., Lorenz, S.J., Scholz, D., Patzold, J., Al-Rousan, S.A., Al-Moghrabi, S.M, 2004. Increased seasonality in Middle East temperatures during the last interglacial period. NatureNature 429, 164–168.
Fok-Pun, L., Komar, P.D., 1983. Settling velocities of planktonic foraminifera; density variations and shape effects. J. Foraminiferal Res. 13 (1), 60–68.
Goldberg, D.E., 1963. Geochronology with ^{210}Pb. In: Symposium on Radioactive Dating. IAEA, Vienna, pp. 121–131.
Goldfinger, C., 2009. Chapter 2B sub-aqueous paleoseismology. Int. Geophys. 95, 119–170.
Goldfinger, C., 2011. Submarine paleoseismology based on turbidite records. Ann. Rev. Mar. Sci. 3 (1), 35–66.
Goldfinger, C., Morey, A.E., Nelson, C.H., Gutiérrez-Pastor, J., Johnson, J.E., Karabanov, E., Chaytor, J., Eriksson, A., 2007. Rupture lengths and temporal history of significant earthquakes on the offshore and north coast segments of the Northern San Andreas Fault based on turbidite stratigraphy. Earth Planet. Sci. Lett. 254 (1–2), 9–27.
Goldfinger, C., Grijalva, K., Burgmann, R., Morey, A.E., Johnson, J.E., Nelson, C.H., Gutierrez-Pastor, J., Ericsson, A., Karabanov, E., Chaytor, J.D., Patton, J., Gracia, E, 2008. Late holocene rupture of the northern San Andreas fault and possible stress linkage to the cascadia subduction zone. Bull. Seismol. Soc. Am. 98 (2), 861–889.
Goldfinger, C., Galer, S., Beeson, J., Hamilton, T., Black, B., Romsos, C., Patton, J., Nelson,

C.H., Hausmann, R., Morey, A., 2017. The importance of site selection, sediment supply, and hydrodynamics: a case study of submarine paleoseismology on the northern Cascadia margin, Washington USA. Mar. Geol. 384, 4–46.
Heaton, T., Köhler, P., Butzin, M., Bard, E., Reimer, R., Austin, W., Bronk Ramsey, C., Grootes, P., Hughen, K., Kromer, B., Reimer, P., Adkins, J., Burke, A., Cook, M., Olsen, J., Skinner, L., 2020. Marine20 - the marine radiocarbon age calibration curve (0–55, 000 cal BP). Radiocarbon.Radiocarbon. 62, 779–820.
Hofstetter, A., 2003. Seismic observations of the 22/11/1995 Gulf of Aqaba earthquake sequence. Tectonophysics. 369 (1–2), 21–36.
Ikehara, K., Kanamatsu, T., Nagahashi, Y., Strasser, M., Fink, H., Usami, K., Irino, T., Wefer, G., 2016. Documenting large earthquakes similar to the 2011 Tohoku-oki earthquake from sediments deposited in the Japan Trench over the past 1500 years. Earth Planet. Sci. Lett. 445, 48–56.
Kanari, M., Niemi, T.M., Ben-Avraham, Z., Frieslander, U., Tibor, G., Goodman-Tchernov, B.N., Wechsler, N., Abueladas, A., Al-Zoubif, A., Basson, U., Marco, S., 2020. Seismic potential of the Dead Sea Fault in the northern Gulf of Aqaba-Elat: new evidence from liquefaction, seismic reflection, and paleoseismic data. Tectonophysics. 793, 228596.
Kelsey, H.M., Hull, A.G., Cashman, S.M., Berryman, K.R., Cashman, P.H., Trexler, J.H., Begg, J.G., 1998. Paleoseismology of an active reverse fault in a forearc setting: the Poukawa fault zone, Hikurangi forearc, New Zealand. Geol. Soc. Am. Bull. 110 (9), 1123–1148.
Klinger, Y., Le Béon, M., Al-Qaryouti, M, 2015. 5000 yr of paleoseismicity along the southern Dead Sea fault. Geophys. J. Int. 202 (1), 313–327.
Klinger, Y., Rivera, L., Haessler, H., Maurin, J.C., 1999. Active Faulting in the Gulf of Aqaba: new Knowledge from the Mw = 7.3 Earthquake of 22 November 1995. Bull. Seismol. Soc. Am. 89 (4), 1025–1036.
Le Béon, M., Klinger, Y., Meriaux, A.S., Al-Qaryouti, M., Finkel, R.C., Mayyas, O., Tapponnier, P., 2012. Quaternary morphotectonic mapping of the Wadi Araba and implications for the tectonic activity of the southern Dead Sea fault. Tectonics. 31, TC5003. https://doi.org/10.1029/2012TC003112.
Lefevre, M., Klinger, Y., Al-Qaryouti, M., Le Béon, M., Moumani, K., 2018. Slip deficit and temporal clustering along the Dead Sea fault from paleoseismological investigations. Sci. Rep. 8 (1), 1–9.
Li, X., Jónsson, S., Cao, Y., 2021. Interseismic deformation from Sentinel-1 burst-overlap interferometry: application to the southern Dead Sea fault. Geophys. Res. Lett. 48, e2021GL093481. https://doi.org/10.1029/2021GL093481.
Masana, E., Martínez-Díaz, J.J., Hernández-Enrile, J.L., Santanach, P., 2004. The Alhama de Murcia fault (SE Spain), a seismogenic fault in a diffuse plate boundary: seismotectonic implications for the Ibero-Magrebian region. J. Geophys. Res.: Solid Earth 109, B01301.
McCalpin, J.P., Nelson, A.R., 2009. Introduction to Paleoseismology. In 1143870963 860846024J. P. McCalpin (Ed.). In: Paleoseismology, 2nd ed. 95. Academic Press, London, UK, pp. 1–27. ISSN 0074-6142.
Moernaut, J., Van Daele, M., Heirman, K., Fontijn, K., Strasser, M., Pino, M., Urrutia, R., De Batist, M, 2014. Lacustrine turbidites as a tool for quantitative earthquake reconstruction: new evidence for a variable rupture mode in south central Chile. J. Geophys. Res.: Solid Earth 119 (3), 1607–1633.
Moernaut, J., van Daele, M., Strasser, M., Clare, M.A., Heirman, K., Viel, M., Cardenas, J., Kilian, R., Ladrón de Guevara, B., Pino, M., Urrutia, R., De Batist, M., 2017. Lacustrine turbidites produced by surficial slope sediment remobilization: a mechanism for continuous and sensitive turbidite paleoseismic records. Mar. Geol. 384, 159–176.
Molenaar, A., Van Daele, M., Vandorpe, T., Degenhart, G., De Batist, M., Urrutia, R., Pino, M., Strasser, M., Moernaut, J., 2021. What controls the remobilization and deformation of surficialsediment by seismic shaking? Linking lacustrine slopestratigraphy to great earthquakes in South–Central Chile. Sedimentology 68, 2365–2396.
Molenaar, A., van Daele, M., Huang, J.J.S., Strasser, M., de Batist, M., Pino, M., Urrutia, R., Moernaut, J., 2022. Disentangling factors controlling earthquake-triggered soft-sediment deformation in lakes. Sediment. Geol. 438, 106200. https://doi.org/10.1016/j.sedgeo.2022.106200.
Monecke, K., Anselmetti, F.S., Becker, A., Sturm, M., Giardini, D, 2004. The record of historic earthquakes in lake sediments of Central Switzerland. Tectonophysics. 394 (1–2), 21–40.
Nakajima, T., Kanai, Y., 2000. Sedimentary features of seismoturbidites triggered by the 1983 and older historical earthquakes in the eastern margin of the Japan Sea. Sediment. Geol. 135 (1–4), 1–19.
Nowaczyk, N.R., 2001. Logging of magnetic susceptibility. In: Last, W.M., Smol, J.P. (Eds.), Tracking Environmental Change Using Lake Sediments. Volume 1: Basin Analysis, Coring, and Chronological Techniques. Kluwer Academic Publishers, Dordrecht, The Netherlands, pp. 155–170.
Orbigny, A.D.d'., 1839. Foraminifères, in de la Sagra R., Histoire physique, politique et naturelle de l'ile de Cuba. A. Bertrand 1–224.
Patton, J.R., Goldfinger, C., Morey, A.E., Romsos, C., Black, B., Djadjadihardja, Y., Udrekh, 2013. Seismoturbidite record as preserved at core sites at the Cascadia and Sumatra–Andaman subduction zones. Nat. Hazards Earth Syst. Sci. 13, 833–867. https://doi.org/10.5194/nhess-13-833-2013.
Patton, J.R., Goldfinger, C., Morey, A.E., Ikehara, K., Romsos, C., Stoner, J., Djadjadihardja, Y., Udrekh, Ardhyastuti, S., Gaffar, E.Z., Vizcaino, A, 2015. A 6600 year earthquake history in the region of the 2004 Sumatra-Andaman subduction zone earthquake. Geosphere 11 (6), 2067–2129. https://doi.org/10.1130/GES01066.1.
Polonia, A., Nelson, C.H., Romano, S., Vaiani, S.C., Colizza, E., Gasparotto, G., Gasperini, L., 2017. A depositional model for seismo-turbidites in confined basins based on Ionian Sea deposits. Mar. Geol. 384, 177–198.
Polonia, A., Melis, R., Galli, P., Colizza, E., Insinga, D.D., Gasperini, L., 2023. Large earthquakes along slow converging plate margins: calabrian Arc paleoseismicity based on the submarine turbidite record. Geosci. Front. 14, 101612.
Purkis, S.J., Ward, S.N., Shernisky, H., Chimienti, G., Sharifi, A., Marchese, F., Benzoni, F., Rodrigue, M., Raymo, M.E., Abdulla, A., 2022. Tsunamigenic potential of an incipient submarine landslide in the Tiran Straits. Geophys. Res. Lett. 49 (4), e2021GL097493.
Ribot, M., Klinger, Y., Jónsson, S., Avşar, U., Pons-Branchu, E., Matrau, R., Mallon, F.L., 2021. Active faults' geometry in the Gulf of Aqaba, southern Dead Sea fault, illuminated by multi beam bathymetric data. Tectonics. 40, e2020TC006443.
Rothwell, R.G., Hoogakker, B., Thomson, J., Croudace, I.W., Frenz, M., 2006. Turbidite emplacement on the southern Balearic Abyssal Plain (western Mediterranean Sea) during marine isotope stages 1–3: an application of ITRAX XRF scanning of sediment cores to lithostratigraphic analysis. Geol. Soc., London, Special Publ. 267 (1), 79–98.
Schmidt, S., Howa, H., Diallo, A., Martín, J., Cremer, M., Duros, P., Fontanier, C., Deflandre, B., Metzger, E., Mulder, T., 2014. Recent sediment transport and deposition in the Cap-Ferret Canyon, South-East margin of Bay of Biscay. Deep Sea Res. Part II 104, 134–144. https://doi.org/10.1016/j.dsr2.2013.06.004.
Schwab, M.J., Werner, P., Dulski, P., McGee, E., Nowaczyk, N.R., Bertrand, S., Leroy, S.A.G., 2009. Palaeolimnology of Lake Sapanca and identification of historic earthquake signals, Northern Anatolian Fault Zone (Turkey). Quat. Sci. Rev. 28 (11–12), 991–1005.
Shamir, G., Baer, G., Hofstetter, A., 2003. Three-dimensional elastic earthquake modelling based on integrated seismological and InSAR data: the Mw = 7.2 Nuweiba earthquake, Gulf of Elat/Aqaba 1995 November. Geophys. J. Int. 154 (3), 731–744.
Shiki, T., Kumon, F., Inouchi, Y., Kontani, Y., Sakamoto, T., Tateishi, M., Matsubara, H., Fukuyama, K., 2000. Sedimentary features of the seismo-turbidites, Lake Biwa, Japan. Sediment. Geol. 135, 37–50.
Thomas, R., Parker, S.T., Niemi, T.M., 2007. Structural damage from earthquakes in the second-ninth centuries at the archaeological site of Aila in Aqaba, Jordan. Basor 346, 59–77.
Tibor, G., Niemi, T.M., Ben-Avraham, Z., Al-Zoubi, A., Sade, R.A., Hall, J.K., Hartman, G., Akawi, E., Abueladas, A., Al-Ruzouq, R, 2010. Active tectonic morphology and submarine deformation of the northern Gulf of Eilat/Aqaba from analyses of multibeam data. Geo-Marine Lett. 30 (6), 561–573.
Usami, K., Ikehara, K., Kanamatsu, T., McHugh, C.M., 2018. Supercycle in great earthquake recurrence along the Japan Trench over the last 4000 years. Geosci. Lett. 5, 11.
Van Daele, M., Cnudde, V., Duyck, P., Pino, M., Urrutia, R., De Batist, M., 2014. Multidirectional, synchronously-triggered seismo-turbidites and debrites revealed by X-ray computed tomography (CT). Sedimentology 61, 861–880.
Van Daele, M., Meyer, I., Moernaut, J., De Decker, S., Verschuren, D., De Batist, M., 2017. A revised classification and terminology for stacked and amalgamated turbidites in environments dominated by (hemi)pelagic sedimentation. Sediment. Geol. 357, 72–82.
Viltres, R., Jónsson, S., Alothman, A.O., Liu, S., Leroy, S., Masson, F., Doubre, C., Reilinger, R., 2022. Present-day motion of the Arabian plate. Tectonics. 41. . e2021TC00713.
Wells, D.L., Coppersmith, K.J., 1994. New empirical relationships among magnitude, rupture length, rupture width, rupture area, and surface displacement. Bull. Seismol. Soc. Am. 84 (4), 974–1002.
Wheatcroft, R.A., 1992. Experimental tests for particle size-dependent bioturbation in the deep ocean. Limnol. Oceanogr. 37 (1), 90–104.
Wils, K., Deprez, M., Kissel, C., Vervoort, M., Van Daele, M., Daryono, M.R., Cnudde, V., Natawidjaja, D.H., De Batist, M, 2021. Earthquake doublet revealed by multiple pulses in lacustrine seismo-turbidites. Geology.Geology. 49, 1301–1306.
Zilberman, E., Amit, R., Porat, N., Enzel, Y., Avner, U., 2005. Surface ruptures induced by the devastating 1068 AD earthquake in the southern Arava valley, Dead Sea Rift, Israel. Tectonophysics. 408 (1–4), 79–99.